Grado en Física
Trabajo de Fin de Grado

Superconducting sensors for X-ray applications

Author:
Sara Malo Núñez

Directors:
Carlos Pobes Aranda
Agustín Camón Lasheras

Departamento de Física de la Materia Condensada
Facultad de Ciencias, Universidad de Zaragoza
25 June 2020

Abstract

Superconducting transition-edge sensors (TES) are used as high sensitivity thermometers in experiments demanding an excellent energy resolution. The X-ray *Athena* mission financed by the European Space Agency (ESA), has the ambition to launch an X-ray telescope incorporating TESs into space for a better understanding of the Hot and Energetic Universe. An optimisation of the response of TESs implies a measurements process using a low energy X-ray emitting source. In particular, this work focuses on evaluating a preliminary implementation of an X-ray acquisition system using a ^{55}Fe source. The study aims to identify possible weak points and optimise the acquisition system. This study will help the Q-MAD (Quantum Materials and Devices) research team belonging to ICMA (CSIC-UZ) to comprehend some open questions about TESs and the acquisition system, among which stands the degradation of the energy spectrum.

Contents

1 Introduction

Historically, visible light has been our primary source of information about the Universe. However, there is enough evidence to state that other bands of the electromagnetic spectrum can give a considerable amount of information. The most energetic and hot objects and phenomena in the Universe are better understood doing an exhaustive investigation of X-rays.

For decades, understanding the formation and evolution of galaxies has been the ambition of significant investigations. The baryonic content of groups and clusters of galaxies is dominated by hot gas, which may represent most of the total baryonic content of the Universe. The peak of black body radiation depends on the temperature, taking place in the X-ray region of the electromagnetic spectrum at temperatures of hot gases. Examining X-rays from the baryonic gas that traces large hot gaseous structures provides a greater understanding of the Hot Universe.

Massive galaxies host a supermassive black hole at their centre, whose mass depends on the properties of the galaxy. The formation and evolution of galaxies is hence tightly influenced by the energy released during the supermassive black hole accretion. Black holes emit radiation mainly in the X-ray region of the electromagnetic spectrum. Examining X-rays from supermassive black holes within massive galaxies provides a greater understanding of the Energetic Universe.

The X-ray *Athena* mission financed by the European Space Agency (ESA), has the ambition to understand the Hot and Energetic Universe at levels well above those currently known, launching an X-ray telescope into space in the early 2030s [1]. The telescope incorporates two different instruments, each of them having its particular scientific programme undertaking different open questions. One of them, the WFI (*Wide Field Imager*), is an X-ray spectroscopic imaging device with low energy resolution offering a fast acquisition image. The other one is the X-IFU (*X-ray Integral Field Unit*), which is a cryogenic X-ray spectrometer holding a vast array of superconducting transition-edge sensors, also known as TES, with a much better energy resolution. Both instruments are equally important because some issues may require maps covering large areas while others may need to study smaller regions with higher energy resolution.

The Q-MAD (Quantum Materials and Devices) research team belonging to ICMA (CSIC-UZ) started developing TESs as a possible backup for the X-IFU instrument. Even though the study of TESs was initially motivated by the X-ray *Athena* mission, the team is currently working on their characterisation for its use in the X-IFU instrument and its application in innovative technological devices, including telescopes operating in other energy ranges.

Some research teams around the globe are working on potential applications of TESs beyond astrophysics and cosmology. These applications include energy dispersive X-ray microanalysis (EDX) [2], time-resolved X-ray absorption fine structure spectroscopy (XAFS) [3] and quantum information [4] amongst others.

1.1 TES devices

A superconducting transition-edge sensor (TES) consists of a thin superconducting film operating in the narrow temperature region between the normal and superconducting state, where the electrical resistance goes from zero to its normal value. The transition between both states is sharp but continuous, and hence a TES works as a thermometer, translating small temperature variations into electrical resistance variations. Their sensitivity makes them suitable quality sensors with high technological potential as they a provide better energy resolution and a faster response than conventional thermal detectors. However, the sharp transition gives rise to greater instability and lower saturation energy [5].

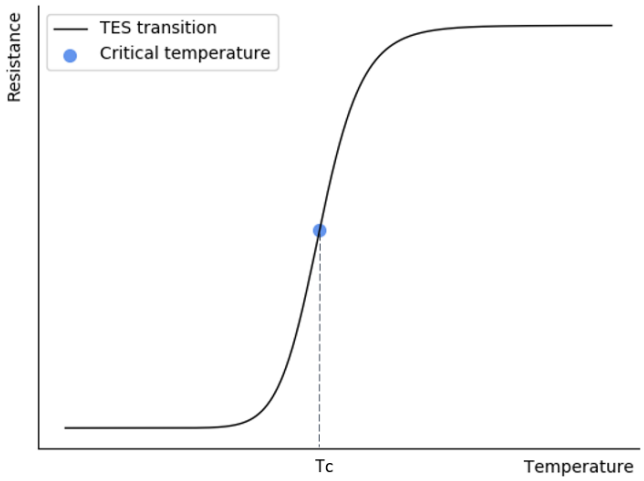

Figure 1: Transition of a superconducting film from the normal to the superconducting state. The sharp phase transition suggests its use as a sensitive thermometer.

A TES connected to an adequate absorber is sensitive enough to detect X-rays, producing temperature variations translated into measurable resistance variations. The TES must be in contact with a heat bath at temperature T_{bath} lower than the critical temperature T_c, to avoid overheating. Whenever the TES temperature increases, it decreases again until equilibrium state transferring energy to the heat bath at a rate given by thermal conductivity G, controlled with a SiN membrane.

The absorber must contain elements with high Z. As a result, the TES used in this particular project combines both Bismuth and Gold. Additionally, to facilitate the translation of small variations in temperature into a measurable signal with high sensitivity, the TES used in this project is assembled using a Mo/Au bilayer.

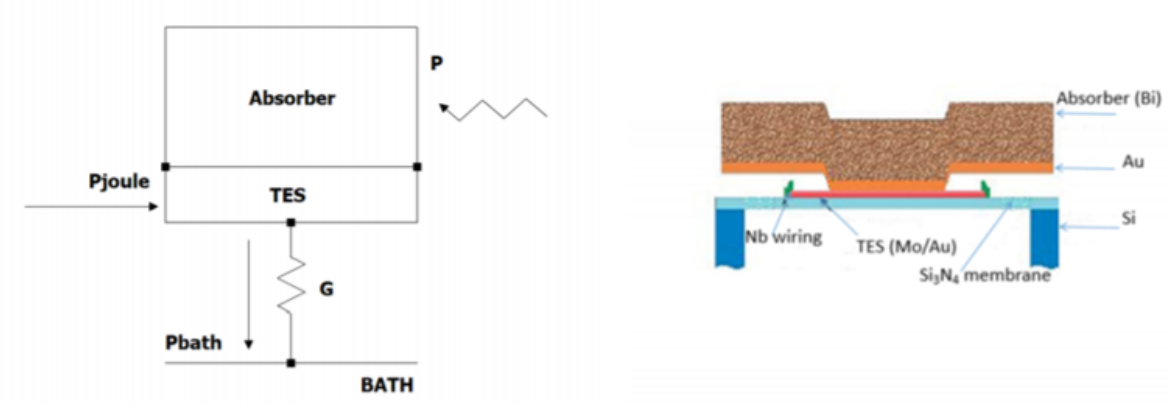

Figure 2: On the left, a diagram of the thermal interaction between the TES and the thermal bath. The TES transfers power to heat bath P_{bath} and receives Joule power P_{Joule} dissipated due to the current going through the TES and a power P associated with an external excitation such as X-rays absorption. On the right, a diagram of the TES.

The range of interest of the *Athena* mission is 1-10 keV, making it convenient to use absorbers with a large atomic number Z. Examples of proper absorbent materials include Bismuth and Gold, which can provide the required quantum efficiency (about 95% at 6 keV) with a few microns of material.

2 Objectives

The characterisation of TESs requires an X-ray emitting source in the low energy range restricted by the *Athena* mission. The most commonly used radioactive source in that energy region is ^{55}Fe emitting 6 keV X-rays. The Q-MAD team has recently implemented the proper set-up to incorporate the named X-ray emitting source in the measurement process.

This project aims to evaluate a first implementation of the pulse acquisition system to identify possible weak points and propose the required improvements. This may have a significant impact on the capability to characterise new TES devices, and hence improve their performance not only on the X-IFU instrument but also on other possible technological applications.

3 Development

The Physics program in the X-IFU instrument determines the minimum requirements of the characteristics of the TES used in this project. Physics required by the *Athena* mission involve the imposition of certain restrictions including a 2.5 eV energy resolution and a 5' diameter field of view, which define the operation temperature, heat capacity and pixel size.

A large area must be covered with good spatial resolution, meaning that it is not possible to use a unique pixel since its thermal capacity would be excessively high and spatial resolution would be lost, therefore determining the size and number of pixels needed. The lateral size of the TES used in this project is 250 x 250 μm^2.

3.1 TES structure

The restriction on the energy resolution of any device characterised by a heat capacity C at a given temperature T depends on thermal fluctuations. These fluctuations give an upper limit of the observed increment in temperature. Thus, for a TES to be sensitive enough, thermal fluctuations must be lower than the energy deposited in the material. Otherwise, they could not traduce small changes in temperature into a measurable signal.

The limitation on the energy resolution is given by $\Delta E = \sqrt{k_B T^2 C}$, and hence it is proper to use an absorber with very small C. The energy resolution expression sets the maximum size of 250 μm width for the absorber of the sensor used in this project. Besides having small C, the sensor must translate the small variations in temperature into a measurable signal with high sensitivity, making it convenient to use a TES with very small T_c. To reach the 2.5 eV energy resolution requirement, T_c must be about 90-100 mK.

Because of the non-existence of pure superconductors with the critical temperature needed, it is necessary to resort to the *proximity effect*, based on the fact that a normal metal deposited on a superconductor with a critical temperature above the required one leads to a change of the critical temperature. Thus implying that a variation on the relative thickness of the normal and the superconducting layer modifies the critical temperature [7].

TESs used in the *Athena* mission are assembled using a Mo/Au bilayer. The research team did an optimisation work previous to the production of the TES used in this project to obtain a thickness combination of the bilayer to reach a critical temperature of 90-100 mK. TESs are usually made with layers of 45 nm Mo and 265 nm Au or 55 nm Mo and 340 nm Au.

As mentioned above, a TES connected to an absorbent material may work as an X-ray detector. The choice of the absorbent material depends on its quantum efficiency for the radiation domain in which measurements are taken.

The *Athena* mission requests an absorption of at least 95% quantum efficiency at 6 keV. The optimum thicknesses that provide the 95% quantum efficiency requirement are 6.3 μm Bi or 3.4 μm Au, given that the attenuation length of Bismuth is 2.1 μm at 6 keV and that of Gold is 1.1 μm. The estimation has been computed considering an exponential attenuation of photons in the absorber

$$1 - 0.95 = e^{-x/l} \tag{1}$$

where, x is the thickness and l is the attenuation length.

When a photon falls upon the absorber, it transfers energy to the detector, leading to a further rise in temperature so that $\Delta T = \Delta E/C$. Since small heat capacities are required to obtain a good energy resolution semiconductor materials are often used. This is because heat capacity depends on the third power of temperature for such materials, while it depends linearly on temperature for conductor materials.

The heat capacity C of the absorbers that ensure a 95% quantum efficiency for the thicknesses calculated in a TES of the same size of that used in this project is 3.6 x 10^{-14} J/K for Bi and 1.5 x 10^{-12} J/K for Au.

Even if Gold has a better quantum efficiency, its heat capacity is excessively large. It is then recommendable to use a combination of both Bismuth and Gold to obtain the quantum efficiency required while minimising the absorber thickness. For testing purposes, the TES used in the first implementation of the pulse acquisiton system holds an Au absorber.

Bismuth absorbers as semimetals do not optimally thermalise energy depositions. A faster thermalisation reduces the dependence between the signal and the position where the photon is absorbed, meaning that energy resolution increases.

The use of a TES as a readout leads to a better energy resolution. Assuming Gaussian noise sources, the theoretical limit of that energy resolution is

$$\delta E_{FWHM} = 2\sqrt{2ln2}\,\sqrt{4k_B T_0^2 \frac{C}{\alpha_I}\sqrt{n/2}} \tag{2}$$

where typical values are $\alpha_I = 100$ and $n = 3$.

Using $T_0 = 100\ mK$ as the TES operation temperature, we obtain that the energy resolution limit is 3.7 x 10^{-17} J for Bi and 2.4 x 10^{-16} J for Au, meaning the theoretical energy resolution limit is 0.23 eV for Bi and 1.5 eV for Au. It is remarkable how small values of C give a much better energy resolution. Even though the theoretical energy resolution of both material meet the *Athena* mission requirements, those values are not feasible in practice, and absorbers must hold Bi.

On account of their high sensitivity, TESs are considerably hard to polarise at the critical temperature. Even so, a mechanism known as *negative electrothermal feedback* let them self-regulate in temperature within the transition region when they suffer excitation from an external source. As a result, TESs stably operate when they are voltage-biased, as shown in figure 3. Potential difference is constant when $R_L << R_0$. Thus, when the sensor is heated and its resistance increases, the intensity of the circuit decreases, maintaining I x R constant. As intensity decreases, so does the dissipated Joule power $P_J = I$ x V, which tends to balance the excitation effect out and so, the TES self-regulates. In this way, changes in intensity provide information about temperature variation, enabling us to reconstruct the energy of the incident signal.

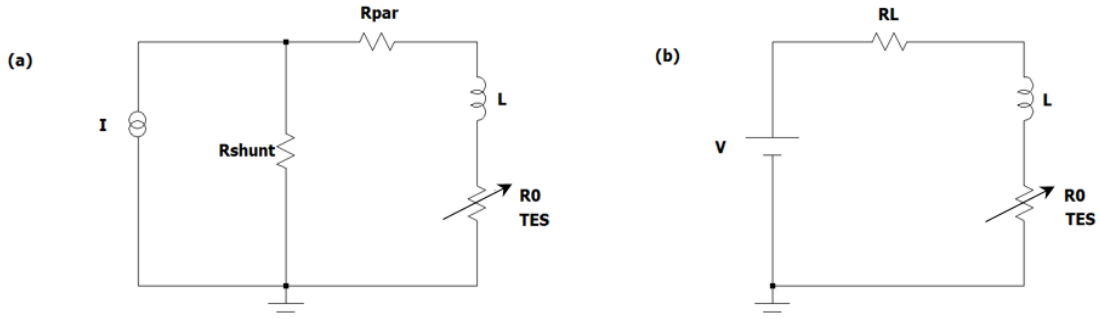

Figure 3: The TES input circuit and a Thevenin-equivalent representation. (a) A bias current is applied to a shunt resistor in parallel with a parasitic resistance, an inductance and a TES. (b) A bias voltage $V = IR_{shunt}$ is applied to a load resistor $R_L = R_{shunt} + R_{par}$, the inductance and the TES.

3.2 TES mathematical description

In this section, we give a mathematical description of a TES using as reference [6]. The aim here is to understand the response of a TES to an energy deposition. The variables under study are the current going through the TES, I_{TES}, and the TES temperature, T_{TES}.

While I_{TES} carries information about the variation of R_{TES} (I_{TES}, T_{TES}) in the presence of the excitation, T_{TES} is the main responsible of R_{TES} variations. For a given operation point, the resistance of the TES remains constant and we denote it as R_0.

Two coupled differential equations describe both parameters, I_{TES} and T_{TES}. To make it simpler, we denote I_{TES}, T_{TES} and R_{TES} as I, T and R respectively.

The *electrical differential equation* is

$$L\frac{dI}{dt} = V - IR_L - IR(T, I) \tag{3}$$

where, L is the inductance, V is the Thevenin-equivalent bias voltage and $R_L = R_{shunt} + R_{par}$ is the load resistance.

The *thermal differential equation* is

$$C\frac{dT}{dt} = -P_{bath} + P_J + P \tag{4}$$

where, C is the heat capacity (of both the TES and the absorber), P_{bath} is the power transferred from the TES to the thermal bath, P_{Joule} is the Joule power dissipated due to Joule effect and P is a power associated with an external energy deposition.

R and P_{bath} are nonlinear terms which complicate the solution of these differential equations. Nonlinear terms can be linearized around their steady-state values under the *small signal* condition. The linearized equations are expressed as a function of the temperature and current logarithmic sensitivities α_I and β_I.

$$\alpha_I \equiv \frac{T_0}{R_0}\frac{\partial R}{\partial T}\bigg|_I = \frac{\partial logR}{\partial logT}\bigg|_I \tag{5}$$

$$\beta_I \equiv \frac{I_0}{R_0}\frac{\partial R}{\partial I}\bigg|_T = \frac{\partial logR}{\partial logI}\bigg|_T \tag{6}$$

The linearized differential equations are

$$\frac{d\delta I}{dt} = -\frac{R_L + R_0(1+\beta_I)}{L}\delta I - \frac{I_0\alpha_I R_0}{LT_0}\delta T + \frac{\delta V}{L} \tag{7}$$

$$\frac{d\delta T}{dt} = \frac{I_0 R_0(2+\beta_I)}{C}\delta I + \frac{\alpha_I P_{J0}/T_0 - G}{C}\delta T + \frac{\delta P}{C} \tag{8}$$

It is useful to define the low-frequency loop gain under constant current

$$\mathscr{L}_I \equiv \frac{P_{J0}\alpha_I}{GT_0} \tag{9}$$

and the natural thermal time constant in the absence of electrothermal feedback

$$\tau \equiv \frac{C}{G} \tag{10}$$

Then, the linearized differential equations become

$$\frac{d\delta I}{dt} = -\frac{R_L + R_0(1+\beta_I)}{L}\delta I - \frac{\mathscr{L}_I G}{LI_0}\delta T + \frac{\delta V}{L} \tag{11}$$

$$\frac{d\delta T}{dt} = \frac{I_0 R_0(2+\beta_I)}{C}\delta I + \frac{1-\mathscr{L}_I}{\tau}\delta T + \frac{\delta P}{C} \tag{12}$$

In the limit of $\mathscr{L}_I = 0$, (11) can be integrated to give an exponential decay of current to steady state with electrical time constant

$$\tau_{el} = \frac{L}{R_L + R_0(1+\beta_I)} \tag{13}$$

In the limit of $\delta I = 0$, (12) can be integrated to give an exponential decay of temperature to steady state with the thermal time constant

$$\tau_I = \frac{\tau}{1 - \mathscr{L}_I} \tag{14}$$

The linearized differential equations are often represented as a matrix

$$\frac{d}{dt}\begin{pmatrix}\delta I \\ \delta T\end{pmatrix} = -\begin{pmatrix}1/\tau_{el} & \frac{\mathscr{L}_I G}{I_0 L} \\ -\frac{I_0 R_0(2+\beta_I)}{C} & 1/\tau_I\end{pmatrix}\begin{pmatrix}\delta I \\ \delta T\end{pmatrix} + \begin{pmatrix}\frac{\delta V}{L} \\ \frac{\delta P}{C}\end{pmatrix} \tag{15}$$

The homogeneous form of (15) is found by taking δV and δP to zero, enabling the decoupling of the equations and hence, the integration of the differential equations to find exponential form solutions.

In the case of the absorption of a photon with instantaneous thermalisation, the impulse corresponds to a delta-function and hence the solution for times $t > 0$, considering that the initial value of temperature change from the impulse is $\delta T(0) = E/C$ and the initial still current is $\delta I(0) = 0$, is

$$\delta I(t) = \left(\frac{\tau_I}{\tau_+} - 1\right)\left(\frac{\tau_I}{\tau_-} - 1\right)\frac{1}{(2+\beta_I)}\frac{C\delta T}{I_0 R_0 \tau_I^2}\frac{(e^{-t/\tau_+} - e^{-t/\tau_-})}{(1/\tau_+ - 1/\tau_-)} \tag{16}$$

$$\delta T(t) = \left(\left(\frac{1}{\tau_I} - \frac{1}{\tau_+}\right)e^{-t/\tau_-} + \left(\frac{1}{\tau_I} - \frac{1}{\tau_-}\right)e^{-t/\tau_+}\right)\frac{\delta T}{(1/\tau_+ - 1/\tau_-)} \tag{17}$$

where we identify the time constants as the *rise time* τ_+ and *fall time* τ_- after a delta-function temperature impulse at time $t = 0$ because $\delta I(t) \propto (e^{-t/\tau_+} - e^{-t/\tau_-})$.

This result is significant because it gives the theoretical form that we are using to fit the experimental pulses

$$\delta I(t) = A\ (e^{-t/\tau_+} - e^{-t/\tau_-}) \tag{18}$$

Both time constants are defined as follows

$$\frac{1}{\tau_\pm} \equiv \frac{1}{2\tau_{el}} + \frac{1}{2\tau_I} \pm \frac{1}{2}\sqrt{\left(\frac{1}{\tau_{el}} - \frac{1}{\tau_I}\right)^2 - 4\frac{R_0}{L}\frac{\mathscr{L}_I(2+\beta_I)}{\tau}} \tag{19}$$

3.3 Experimental setup

In this section, we describe the single-pixel TES detector used in this project to detect X-rays emitted by a ^{55}Fe radioactive isotope.

Energy resolution improves as temperature decreases. To reach temperatures about 100 mK, a dilution refrigerator containing a ^{3}He/^{4}He mixture is used. The TES absorbs the incident photon energy, and hence the temperature of the electronic cloud raises, producing a breaking of Cooper Pairs. The addition of unpaired electrons leads to an increment of the resistance. Thus, the TES must be connected to a thermal bath. The TES must also be magnetically isolated. Magnetic isolation is achieved using two different elements. The first one is a μ-metal capsule with high magnetic permeability acting as a carrier of field lines. The second one is a Pb capsule fanning every other field when it acts as a superconductor. An opposite-field generated by a coil incorporated in the TES holder cancels the remanent magnetic field inside the capsules.

The TES holder is placed in front of the X-ray source and is coupled to a bias circuit and an external readout circuit containing a SQUID (*Superconducting Quantum Inference Device*).

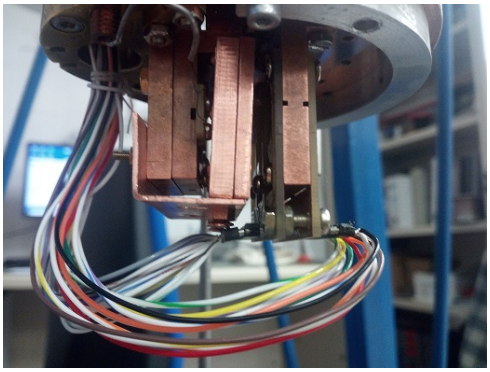

Figure 4: X-ray source holder and TES holder.

When the current going through the TES changes, an inductance L_{in} generates a magnetic field which connects with the SQUID. The total inductance L is the sum of the coupling inductance L_{in} and some parasitic inductances. The magnetic field going through the SQUID must be an exact number of magnetic flux quantum. Since the generated field is not necessarily quantised, the SQUID generates a field, so the sum of both contributions is. The current induced in the SQUID generates a potential difference, which is later amplified and measured in V_{out}. Finally, the feedback path containing a resistance R_f and a coil L_f linearises the SQUID response.

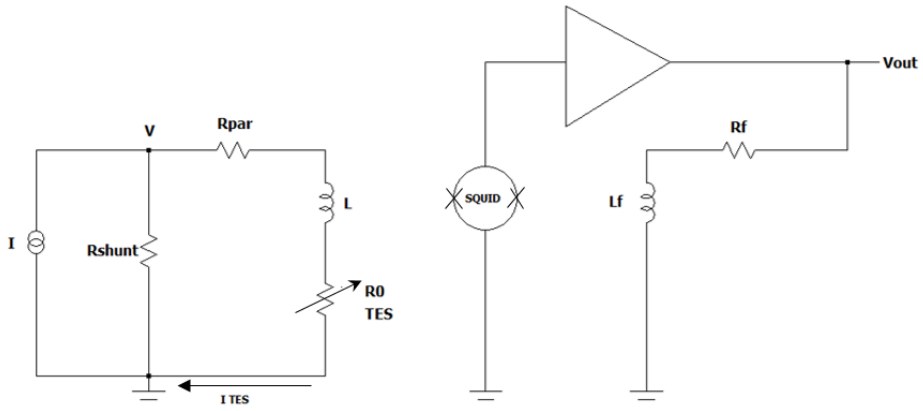

Figure 5: Configuration of the bias and readout circuits of the TES.

We can identify changes in I_{TES} by measuring V_{out}. Both variables are related as follows

$$V_{out} = \frac{M_{in} R_f}{M_f} I_{TES} \tag{20}$$

where, M_{in} and M_f are the mutual inductances.

An acquisition system with a PXI-5922 digitizer card reaching a resolution of 24 bits at 50KS/s or 16 bits at 15MS/s is coupled to the external readout circuit containing the SQUID, storing V_{out} values. The digitizer card is directly connected to the computer, providing the information needed to estimate some relevant parameters of the pulses. Since the acquisition system is programmable, it enables us to set some measurement factors depending on the parameters of the pulses we are interested in, such as the time window, the sampling frequency or the trigger.

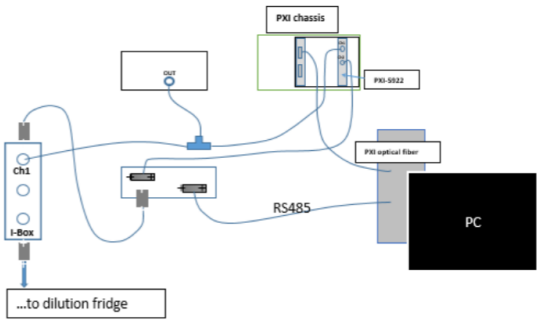

Figure 6: Diagram of the acquisition system.

3.4 X-ray source

^{55}Fe is a radioactive isotope that decays by electron capture to ^{55}Mn. The half-life of the process is $T_{1/2} = 2.747$ years, and hence the disintegration constant is $\lambda = 8$ x 10^{-9} s^{-1}.

$$\lambda = \frac{ln2}{T_{1/2}} \tag{21}$$

This process releases Auger electrons of 5.19 keV with a probability of about 60%. The energies of the emitted X-rays are so similar that sometimes it is considered that the process releases mono-energetic X-rays of 6 keV with a probability of about 28%. The other 12% is for low energy Auger electrons and photons from minor transitions.

	Energy (keV)	Relative intensity	Photons per 100 disintegrations
K_{α_2}	5.88765	51	8.45
$K_{\alpha 1}$	5.89875	100	16.57
K_{β}	6.49045	20.5	3.40

Table 1: Primary X-rays released by the ^{55}Fe source [8].

The ^{55}Fe source used in this project had an initial activity of 1.85 MBq. The team bought the source about two years before the measurement process. Thus, the activity when the data was obtained was about 1.12 MBq or 1.12 x 10^6 disintegrations per second.

$$A = A_0 e^{-\lambda t} \tag{22}$$

The solid angle at which photons are detected by the TES is $\Omega = 1.56$ x 10^{-4}.

$$\Omega = \frac{S}{d^2} \tag{23}$$

where S = 62500 μm^2 is the TES area and $d = 2$ cm is an estimation of the distance between the source and the TES.

The number of X-rays emitted per disintegration is about 0.28, meaning that the rate of photons reaching the detector is about 3.8 photons per second. As mentioned above, the theoretical quantum efficiency of the absorber is 95%, meaning that the rate of photons absorbed by the detector is 3.6 photons per second.

The rate given is a rough estimation because of the non-precise measures of the geometrical factors and the possible absorption of photons within the source holder. By that mean, the rate of photons absorbed by the detector must be measured experimentally.

4 Results

In this work, we have analyzed data from a preliminary run in order to make a first evaluation of the X-ray acquisition system. The initial objective included the evaluation of possible improvements to this acquisition system with new measurements, which could not be performed due to the laboratory shutdown. The analysis has allowed nonetheless to elaborate a list of improvements to implement in the near future. We begin with a pre-analysis of the events in order to filter out anomalous ones, which in this case amounts to a significant fraction of the total events.

The run under study consists of 19993 data files, each of them including the output voltage measured in a time window of 0.02 seconds.

4.1 Filtering of events

As mentioned above, it is necessary to filter the events to separate those containing one pulse that can be fitted to the theoretical form given in equation (18). Since one of the final purposes of the project is to obtain the energy spectrum of the source, we necessarily need to study the area of each event. Before doing so, we are going to plot a good event and visualize the parameters under study.

The parameters used to filter the events are the DC level, the amplitude and the area. We have defined here DC level as the voltage mean value in the range from 5% to 95% of the pretrigger. For the amplitude and the area, we have followed the general definition. The amplitude is the difference between the voltage maximum and the DC level, and the area is the sum over the pulse minus the DC level. Even though the mentioned estimators are non-optimum, they are enough to perform a first filtering of the pulses.

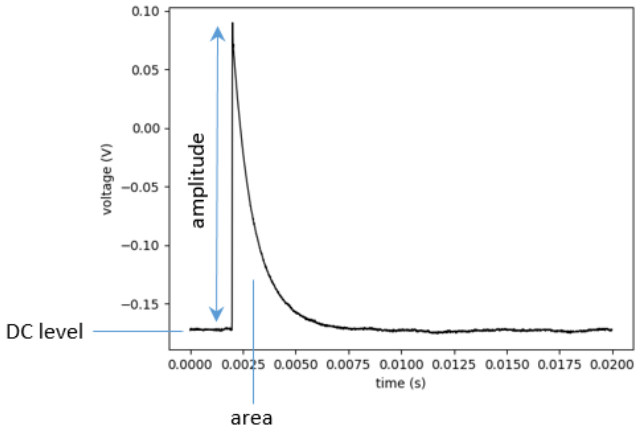

Figure 7: Plot of the voltage as a function of time corresponding to a good event.

A scatter plot of the area and the amplitude can be useful to examine whether the files contain similar events. A glance at the plot is enough to determine a wide variety of events, including some with negative area. The negative area of some events is due to the initial DC value being higher than the final one. The existence of events with negative area can be explained as an abrupt change in the DC level or as a pulse detected before the previous one had vanished entirely.

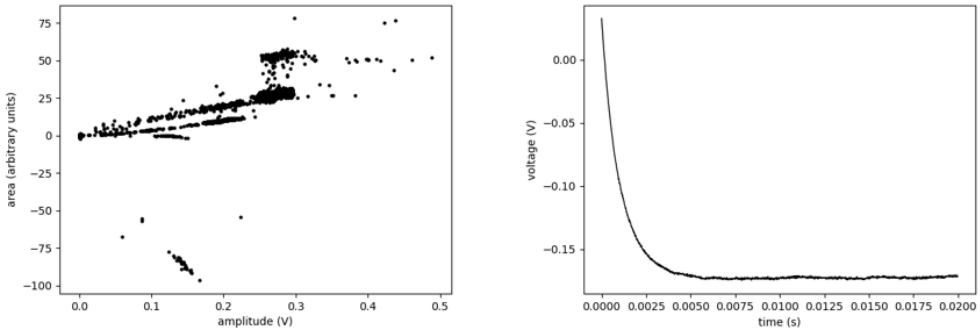

Figure 8: The plot on the left is a scatter plot of the area and the amplitude. The plot on the right represents the output voltage of one of the events corresponding to one of the points with a negative area.

The area is only one of the many parameters that one can use to filter the set of events stored in the computer. Another parameter we can examine is the DC level. Studying the mean DC level of the events, we find that at certain points in the acquisition process, the mean DC value changed drastically.

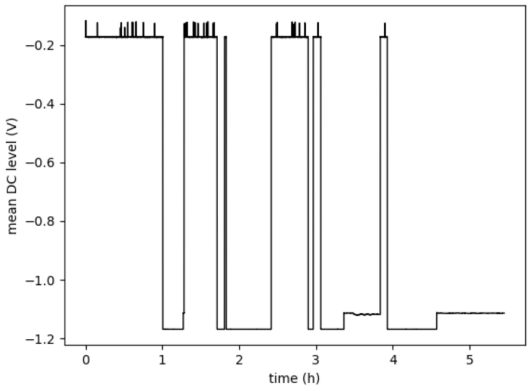

Figure 9: Plot of the mean DC level as a function of time.

A deeper study of both regions of pulses is needed to identify which ones have the form given by equation (18). Plotting events of both groups, we find that events with a mean DC level up to -1V have a positive area but are truncated.

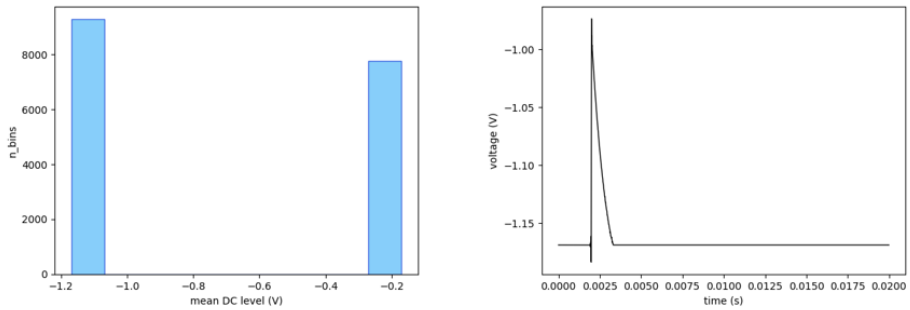

Figure 10: The plot on the left is a mean DC level distribution. The plot on the right represents the output voltage of one of the events corresponding to the points with mean DC level below -1V.

More than half of the events have been removed at this point, meaning that the efficiency of the acquisition system is remarkably low. One reason to explain the low efficiency is the lack of diagnosis criterium in the acquisition process, meaning that the system is not able to identify changes in the DC level. As a result, including a checking system that resets the SQUID when it identifies a change in the DC level could upgrade the acquisition system. This improvement on the acquisition system guarantees the storing of already DC filtered events in the computer, leading to a faster acquisition process.

As suggested above, a scatter plot of the area and the amplitude of the remaining events can be helpful to distinguish regions of different types of events. We are going to analyse the scatter plot of the filtered events for further understanding.

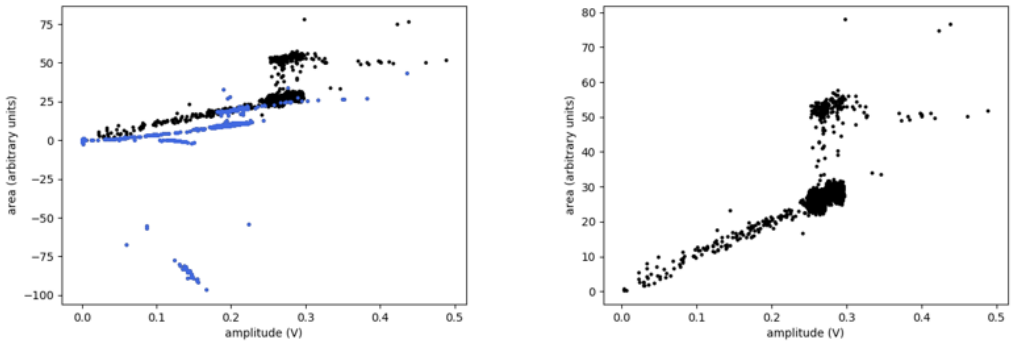

Figure 11: The scatter plot on the left is a plot of the area and the amplitude of the unfiltered data. The blue points correspond to the removed events. The scatter plot on the right corresponds to the filtered data.

We can clearly differentiate two regions with a high density of events. Both regions have the same range of values for the amplitude. However, the area of both regions of events differs a factor 2, suggesting that these regions correspond to events having one and two pulses.

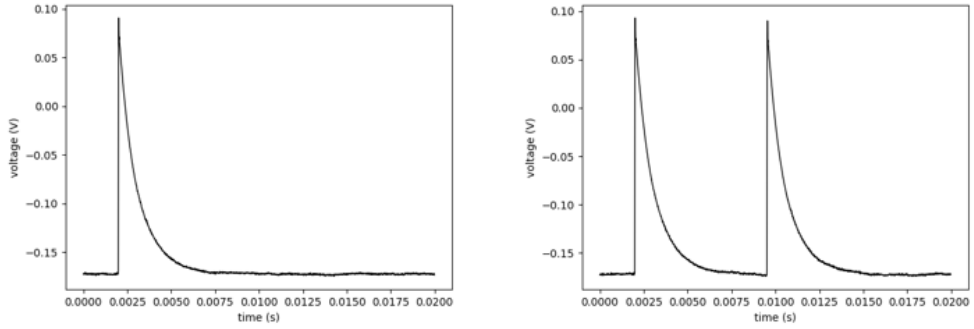

Figure 12: The plot on the left represents the output voltage of one of the events corresponding to the region of points with area around 25. The plot on the right represents the output voltage of one of the events corresponding to the region of points with area around 50.

Since we are interested in fitting the pulses to the theoretical form given in equation (18) it is convenient to arrange the events in those corresponding to one pulse and those corresponding to pileups. There are 7749 files at this point, 7523 contain one pulse, and 226 are pileups.

The next step is to fit the filtered events to obtain the optimum parameters in equation (18). It is useful to plot some events with their fit in the same graph to check that indeed the events under study have the expected shape.

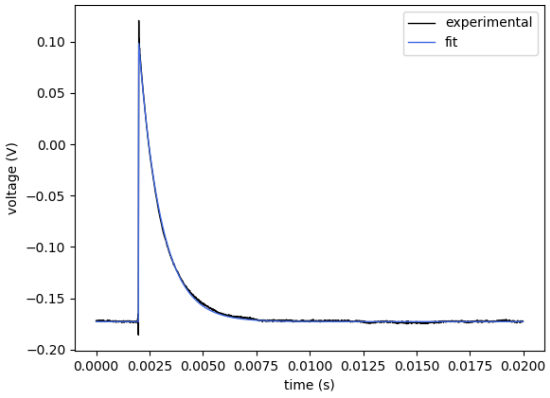

Figure 13: Experimental pulse fitted to the theoretical form.

4.2 Energy spectrum

The aim is to compute the energy spectrum of the source to calibrate the acquisition system. The study of the energy spectrum starts with a comparison of the estimated area distribution with the expected energy distribution.

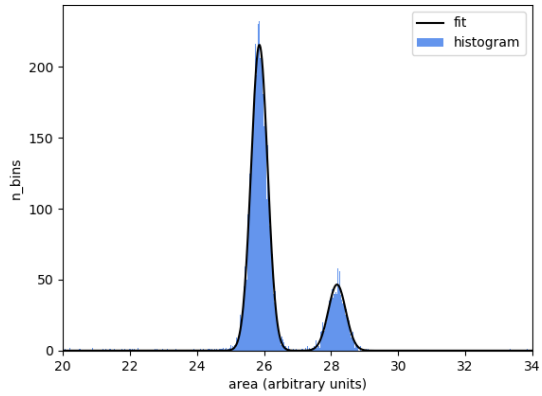

Figure 14: Area distribution fitted to two Gaussian curves.

The area distribution suggests the existence of two groups of pulses with different area, being the group of pulses with the smallest area the predominant one. From the Gaussian fit of the peaks, we obtain that the mean area of the dominant group is 25.87 ± 0.25 and the area of the other group is 28.19 ± 0.26. As a result, the width of the Gaussians compared to the position is about 1 %, meaning that the resolution is not enough to distinguish between X-rays with energies 5.88765 and 5.89875 keV as their difference is 0.2 %.

By that mean, the first peak corresponds an energy equal to the weighted mean of the two populations of X-rays. As mentioned in table 1, the relative probability of X-rays with energy 5.88765 keV is 51 while that of X-rays with energy 5.89875 keV is 100.

$$E = \frac{5.88765 \cdot 51 + 5.89875 \cdot 100}{100 + 51} = 5.89500\ keV \tag{24}$$

Given that the first peak corresponds to energy 5.89500 keV and assuming that the zero of the energy and the area coincide, we obtain that the second peak corresponds to energy 6.424 keV. The second peak corresponds to energy 6.49045 keV, and hence the relative error is 1%. Even though linearity is not ideal, real data fits well with the estimation given that the operation point is not optimised.

We obtain an energy spectrum with two peaks at 5.895 ± 0.057 keV and 6.424 ± 0.059 keV. As a result, the energy resolution is about 55 eV, more than one order of magnitude above the 2.5 eV requirement of the *Athena* mission.

The approach now is to explain the low energy resolution that does not enable us to distinguish between the 5.88765 keV and the 5.89875 keV peaks. One possible explanation could be the presence of oscillations in the position of the low energy peak with time. A plot of the area of the peak as a function of time can be useful to determine the existence of oscillations in the peak position, which would cause a low energy resolution.

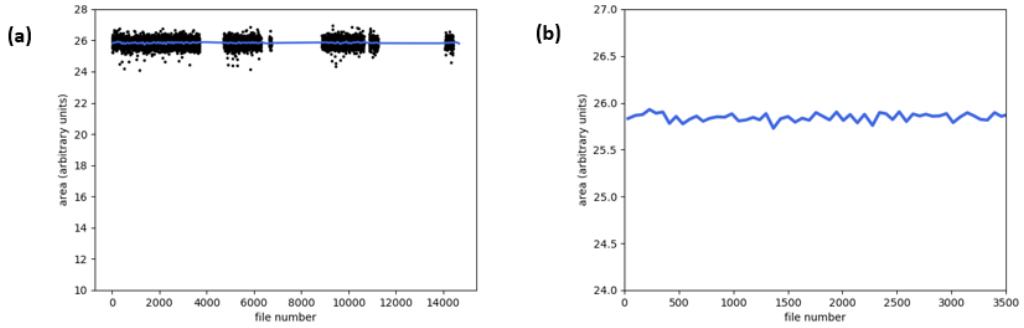

Figure 15: The plot on the left is the mean area of the low energy peak as a function of the file number. Black dots represent the original data, and the blue line is the result of averaging 40 following points repeatedly. The plot on the right is a zoom-in of the blue line.

The distribution of areas is the projection of this plot in one dimension, meaning that time information is lost. A zoom of figure 15a reveals that the fluctuation of the peak does not change with time. By this mean, we cannot attribute the low energy resolution to variations in the peak area as a consequence of drifts in temperature of the order of several minutes during the measurement process.

A more in-depth study of figure 15b shows that the line corresponding to the average of 40 consecutive points is not straight but has small fluctuations. A reason explaining this tendency could be the presence of a hidden frequency. A plot of the Fourier transform of data in figure 15a for file number up to 3500 can be helpful to confirm the existence of a given frequency. A plot of the Fourier transform of a signal with a distinct frequency shows a peak at that particular frequency.

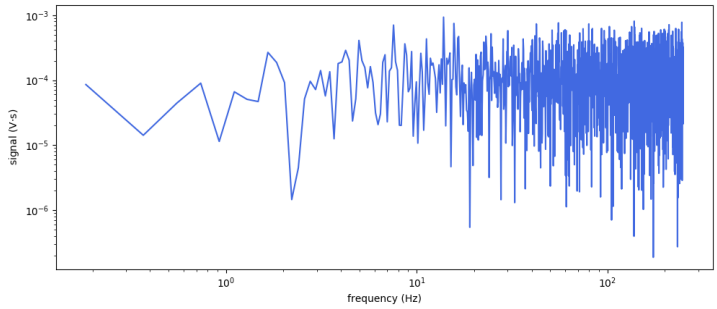

Figure 16: Log-log plot of the Fourier transform of the area as a function of frequency.

The original signal has the same amplitude at all frequencies, meaning that the frequency spectrum is Gaussian, and hence the low energy resolution is not caused by a hidden frequency. This implies that the pulse to pulse condition is degrading the energy resolution. Thus, it is necessary to improve stability in temperature in times of the order of the acquisition rate, vibrations and others.

4.3 Parameters of response to an energy deposition

We are going to estimate now the *rise time* τ_+ and the *fall time* τ_- to draw some information about the TES response to an instantaneous energy deposition, starting with the *fall time*.

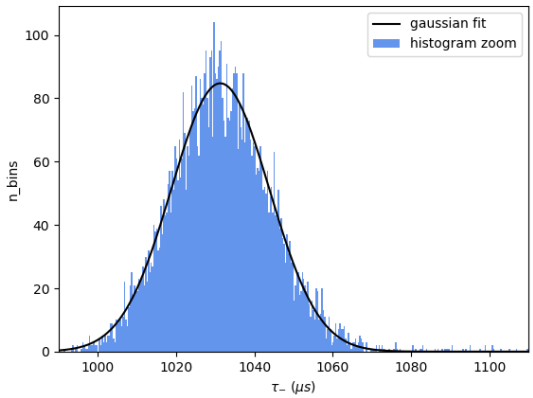

Figure 17: Fall time distribution fitted to a Gaussian curve.

Some pixel designs are being considered for the X-IFU instrument now. The *fall time* ranges from 306 μs in the fastest design to 788 μs in the slowest one. The *fall time* of the pixel used in this project is estimated to be $\tau_- = 1031 \pm 13$ μs, slightly above the specifications given by the *Athena* mission. Even so, the order of magnitude agrees, and the obtained value is reasonable given that the operation point of the system is not optimised. The *fall time* could then be reduced by optimising the operation point. However, it could also be necessary to adjust the pixel design to accomplish the parameters required by the mission.

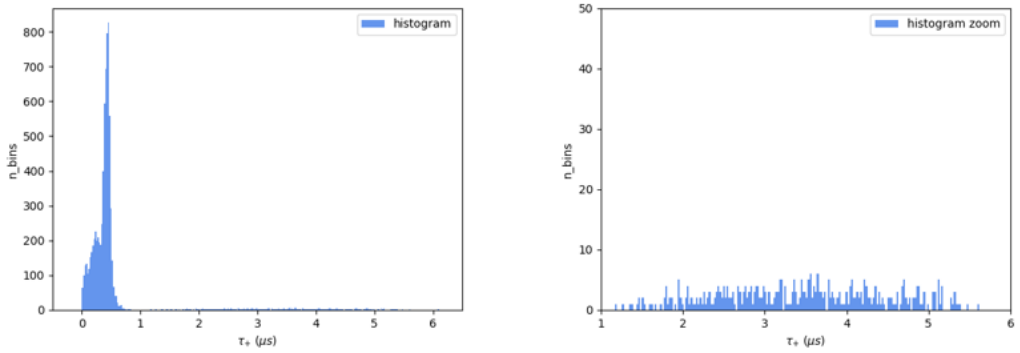

Figure 18: The plot on the left is a rise time distribution. The plot on the right is a zoom of the tail observed in the rise time distribution.

The *rise time* distribution has a peak around 0.4 μs and a tail up until 6 μs. A study of the initial time t_0 can give some information on the origin of the tail. A scatter plot of both parameters shows a strong correlation between the tail of the *rise time* distribution and a specific value of the initial time.

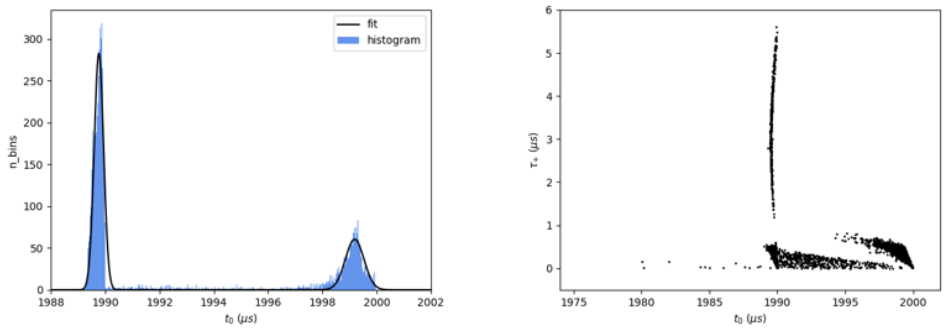

Figure 19: The plot on the left is the initial time distribution fitted to two Gaussian curves. The plot on the right is a scatter plot of the rise time and the initial time.

The initial time distribution suggests the existence of two groups of pulses with different initial times. From the Gaussian fit of the peaks, we obtain that the mean initial time of the first population is 1989.89 $\pm$ 0.17 μs and the mean initial time of the second population is 1999.20 $\pm$ 0.34 μs. The window time is 0.2 seconds and data is measured at 100 kHz, meaning that the best possible time resolution is 10 μs. That value is comparable to the distance between both peaks, suggesting that the digitalisation causes the existence of two populations of t_0.

A plot of a pulse corresponding to each of the populations of t_0, reveals similar rise times. The digitalisation effect together with the trigger effect and the fast rise time translates into two different t_0 populations. An improvement of the trigger system is not plausible at the moment as it has a high cost because it refers to the need for new hardware.

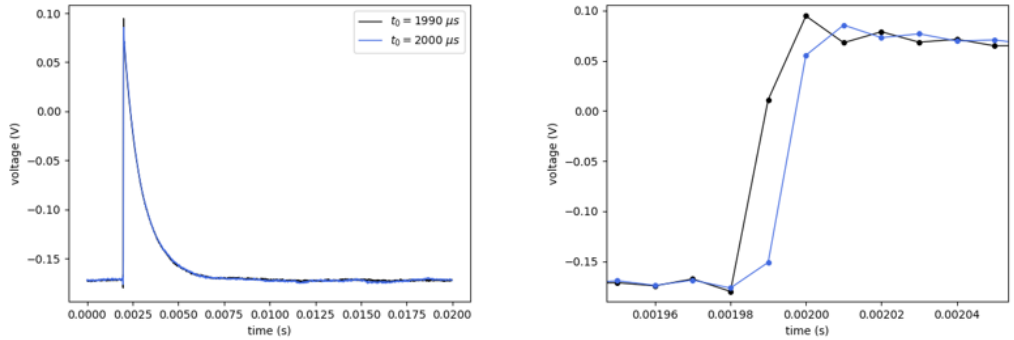

Figure 20: The plot on the left correspond to a pulse of each population of t_0. The plot on the right is a zoom-in revealing the different rise times.

To evaluate the possible effect of these two t_0 populations on energy resolution, we have also constructed the energy spectrum for only one of the t_0 populations to compare the energy resolution obtained with the one of the whole spectrum. The lowest energy peak is the one we are interested in since the low energy resolution does not allow us to distinguish two different peaks within it.

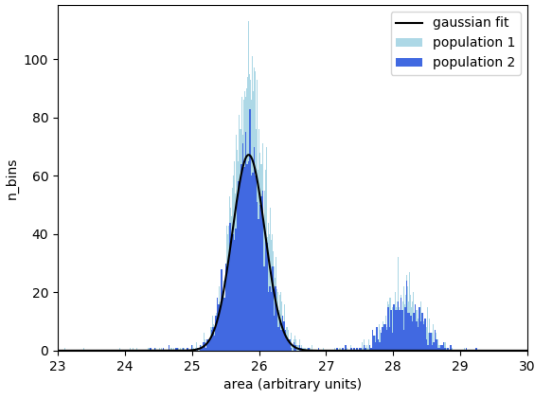

Figure 21: Area distribution for each population of τ_0.

From the Gaussian fit, we obtain that the mean area of the population giving better energy resolution is 25.85 ± 0.24. The percentage of energy resolution in the original estimation of the whole spectrum was 2.28 %, while we are now getting an energy resolution of 2.19 %. Thus, the effect of having two t_0 populations is not meaningful, but we could try to reduce it acquiring pulses at higher frequencies.

4.4 Photon absorption rate

A run of 20 data files was acquired to measure the photon absorption rate. The files contain the output voltage measured in a time window of 4 seconds so that each file has more than one pulse.

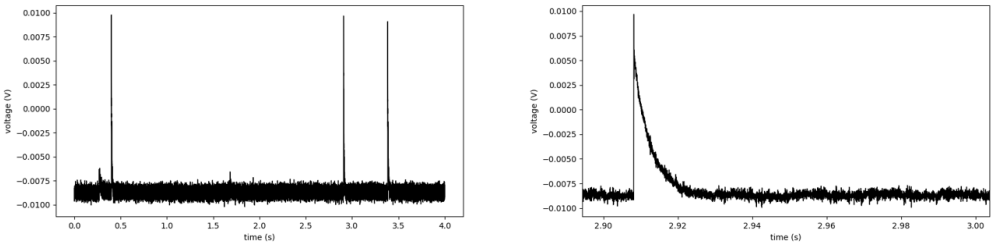

Figure 22: The plot on the left represents the output voltage during one of the 4 seconds time window files. The plot on the right is the zoom of one of the pulses of the file.

One way to calculate the rate is counting the pulses in each file and average out the results. The mean number of pulses every 4 seconds is 6.67 ± 0.67, meaning that the rate of photons absorbed by the detector is 1.67 ± 0.17 photons per second.

Another option is measuring the time between two consecutive pulses. A histogram of those values should decay exponentially. Thus, fitting the histogram to

$$f(\Delta t) = A\ e^{-\lambda \Delta t} \tag{25}$$

gives an estimation of the rate λ. The result is not particularly accurate because of the lack of statistics. Using this method, we obtain that the rate of photons absorbed by the detector is 1.97 ± 0.24 photons per second.

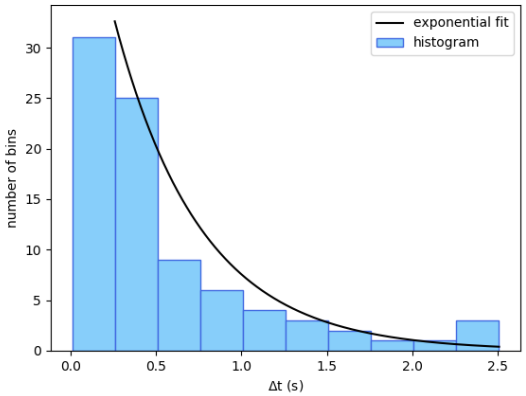

Figure 23: Δt distribution fitted to an exponential curve that provides the rate value.

Experimental values for the rate are compatible but much lower than the theoretical one. A possible interpretation of this result is that part of the low energy photons emitted by the source are not able to get out of the source capsule and are absorbed before reaching the TES. When the TES and the source are not perfectly adjusted, the collimated X-ray beam does not reach the sensor, and hence even the smallest asymmetry can drastically reduce the rate of photons reaching the sensor.

We are now going to estimate the photon rate absorption for the run of 19993 files. The time window of each file is much lower in this case, meaning that in a Δt distribution, we would not be able to see an exponential decay. Thus, we need to estimate the proportion of files containing more than one pulse.

The probability of having at least two pulses in the t_f time window is

$$P(t < t_f) = \int_0^{tf} \lambda e^{-\lambda t}\ dt = 1 - e^{-\lambda t_f} \tag{26}$$

Even though the time window is 0.020 s, we are considering t_f as 90% of the time window because the trigger is at 10%. That is, $t_f = 0.018\ s$.

Given that the proportion of pileups is

$$P = \frac{226}{7749} = 0.029$$

and solving for λ, we obtain that the rate of photons absorbed by the detector is 1.64 ± 0.11 photons per second.

The rate measured in this run is comparable to the rate measured in the other run, and is again much lower than expected. Thus, explaining the needing of measuring the rate of absorbed photons experimentally.

4.5 Dead time of the acquisition system

We are going to estimate the dead time of the run consisting of 19993 data files, given that the acquisition system was measuring during 19632 seconds.

The effective rate gives an estimation of the mean dead time of the acquisition system since it is defined as the number of events per unit time.

$$\frac{19993}{19632\ s} = 1.02\ s^{-1}$$

The effective rate is considerably lower than the rate estimated using experimental data, giving a reason to presume that the dead time of the acquisition system is larger than required.

To obtain the dead time we first need to calculate the time between events considering both the legitimate and the acquired events. The time between consecutive legitimate events is

$$\Delta T = \frac{1}{1.64\ s^{-1}} = 0.61\ s$$

while the mean time between consecutive acquired events is

$$\Delta T = \frac{1}{1.02\ s^{-1}} = 0.98\ s$$

The mean time consumed by the data acquisition system per event is the difference between the times calculated above. As a result, we obtain the following value for the mean dead time

$$< T_{dead} > = 0.98 - 0.61 = 0.37\ s$$

The number of events stored by the computer is 19993, meaning that the total dead time is about two hours. Therefore, suggesting that the acquisition system is not optimised. Compared to the acquisition time of about five and a half hours, we can state that the system is consuming much time, and hence we can update it to store more data during the same acquisition time.

5 Conclusions

In this work, we interpreted the measurements of a preliminary implementation of an X-ray acquisition system, filtering the events and analysing those with the form given by the derived mathematical expression. The results made clear that the characterisation of a TES is not feasible with the available acquisition system as it degraded the energy resolution and hence restricted the differentiation of the peaks of the ^{55}Fe energy spectrum.

For the future, we are exploring the possibility of including a checking system that resets the SQUID when it identifies a change in the DC level. This improvement on the acquisition system would lead to a better efficiency of good events.

In this particular run, the events were analysed during the acquisition process, leading to a high dead time. This problem will be solved for future runs, as the events will be analysed afterwards, and hence the dead time is expected to be reduced substantially. The impact of the trigger will also be evaluated in future runs using a higher acquisition frequency, aiming to find a solution for the energy resolution loss as a consequence of the trigger effect.

In addition to the mentioned changes in the acquisition system, it would also be necessary to improve stability in temperature, vibrations and others to meet the requirements of the X-IFU instrument. In the next run, the Low-Temperature Research Team will incorporate a temperature controller, expecting to evaluate the temperature effect in the measured data. However, other improvements including better vibration stability require a new set-up, as the available one cannot be upgraded at such levels.

References

[1] Barcons X. et al. *Athena: the X-ray observatory to study the hot and energetic Universe.* Journal of Physics: Conference Series **610** (2015) 012008

[2] Wollman D.A., Irwin K.D., Hilton G.C., Dulcie L.L., Newbury D.E. and Martinis J.M. *High-resolution, energy-dispersive microcalorimeter spectrometer for X-ray microanalysis.* Journal of Microscopy **188** (1997) 196-223.

[3] Bunker G. *Introduction to XAFS: Practical guide to X-ray absorption fine structure spectroscopy.* Cambridge University Press (2010).

[4] Miller A.J., Nam S.W., Martinis J.M. and Sergienko A.V. *Demonstration of a low-noise near-infrared photon counter with multiphoton discrimination.* Applied Physics Letters **83** (2003) 791-793.

[5] Kinnunen K. *Studies of transition-edge sensor physics: thermal models and noise.* University of Jyväskylä. Research report 13/2011. ISSN 0075-465X.

[6] Irwin K.D. and Hilton G.C. *Transition-edge sensors.* Applied Physics Letters **99** (2005) 63-149.

[7] Martinis J.M., Hilton G.C., Irwin K.D. and Wollman D.A. *Calculation of T_c in a normal-superconductor bilayer using the microscopic-based Usadel theory.* Nuclear Instruments and Methods in Physics Research A 444 (2004) 23-27.

[8] Bé M.M. and Chisté V. *Table de Radionuclèides.* LNE - LNHB/CEA (1994-2006)